SIMPLE SOLUTIONS TO EQUILIBRIUM CUMULUS REGIMES IN THE CONVECTIVE BOUNDARY LAYER

J. Schalkwijk[1*], H.J.J. Jonker[1] and A.P. Siebesma[1,2]
[1]Delft University of Technology, Delft, The Netherlands
[2]Royal Netherlands Meteorological Institute, Delft, The Netherlands

Abstract

A modeling framework is developed which extends the mixed layer model to cloudy convection, closed using linearity of fluxes throughout the boundary layer. The presented framework allows for the evaluation of equilibrium states on the basis of the current environmental conditions. This equilibrium state is largely independent of the initial conditions, and therefore presents an asymptotic tendency which might help deepen our understanding of the boundary layer dynamics. Using the profile of the buoyancy flux, cloudless, coupled and decoupled regimes can be distinguished *a priori*. These predictions are tested by comparison to a large number of independent Large-Eddy Simulations, and are found to be in good agreement with the simulation results.

1. INTRODUCTION

Boundary layer clouds play an important role in both the dynamical and radiative properties of the boundary layer, controlling to an important extent the height, the efficiency of vertical transport and the transparency of the boundary layer. However, these clouds are also notoriously hard to model due to the high resolution needed to resolve boundary layer turbulence. Stratocumulus cloud decks require high vertical resolution to resolve cloud-top entrainment, and properties of cumulus clouds are also sensitive to horizontal grid resolution due to their inhomogeneity.

Understanding of cumulus clouds has increased significantly over the past decades, in part due to Large Eddy Simulations (LES, e.g. Deardorff, 1970), which allowed many numerical studies to be performed on detailed cloud processes. Especially understanding the cloud-environment interactions (Heus and Jonker, 2008; Paluch, 1979; Reuter and Yau, 1987; Siebesma and Holtslag, 1996) has been a popular topic over many years, enhancing our understanding of cumulus clouds and improving parameterizations. However, the behavior of the cumulus-capped boundary layer as a whole and the interplay with large scale tendencies and forcings is still poorly understood. This is further emphasized by studies on the wide spread of cloud-climate feedbacks (Bony et al., 2006; Dufresne and Bony, 2008), revealing the large uncertainties associated with the feedback behavior of low clouds.

*Corresponding author address: Jerôme Schalkwijk, Delft University of Technology, Delft, The Netherlands (J.Schalkwijk@tudelft.nl)

For this reason, this work attempts a very simple modeling approach, regarding the boundary layer as a simple dynamical system. Starting with the mixed layer model for clear convective situations, building on the work of Lilly (1968); Tennekes (1973) and, more recently, van Driel and Jonker (2011); Vilà-Guerau de Arellano et al. (2004), the model is further elaborated to include a cloud layer, working in the line of Stevens (2006), Neggers et al. (2006) and Stevens (2007). The goal of this exercise is to set up a framework in which one can study the response of cumuliform clouds to large-scale atmospheric forcings and surface properties, minimizing complications by eliminating as many competing complexities as possible. Note that in doing this, a somewhat different approach is chosen than in detailed bulk studies like, for example, Bretherton and Park (2008) and Nuijens and Stevens (2011), which propose more realistic models which focus on the dynamical temporal response of the cloud layer, where we focus on the equilibrium solutions.

2. BULK MODELING

In order to keep our model as simple as possible, this work will consider a non-advective boundary layer, i.e. $\overline{u} = \overline{v} = 0$, with horizontally homogeneous turbulent fluxes and sources. In these conditions, the conservation equation for an arbitrary scalar ψ becomes a one-dimensional equation:

$$\frac{\partial \overline{\psi}}{\partial t} + \overline{w}\frac{\partial \overline{\psi}}{\partial z} = -\frac{\partial \overline{w'\psi'}}{\partial z} + S_\psi \tag{1}$$

where incompressibility is assumed. This equation is the starting point for many (mixed-layer) models of the turbulent boundary layer. Note that not all assumptions are strictly necessary: an equivalent equation can be found for an advective case with nonzero geostrophic wind in Stevens (2006).

2.1 *General bulk modeling*

A bulk model is found when the height dependence in equation (1) is integrated out. For this purpose, we follow the notation of Stevens (2006) and define the bulk average

$$\widehat{\psi} = \frac{1}{h^+}\int_0^{h^+} \overline{\psi}\, dz \tag{2}$$

with h the height of the boundary layer. Hence, $\widehat{\psi}$ is the boundary layer average value of ψ. Integration is performed from 0 to h^+ where $h^+ = \lim_{\epsilon\to 0} h + \epsilon$ to include the possibility of a discontinuity at the boundary layer top.

For simplicity, we assume a constant vertical velocity profile which we denote by the subsidence velocity defined downward: $\overline{w} = -w^s$, and constant sources. Note that the derivation is also possible for a case of constant (or even generalized) divergence ($\overline{w} = -Dz$) and non-constant sources, as is shown in the appendix. For now, the integration of equation (1) yields the following equation

$$h\frac{\partial\widehat{\psi}}{\partial t} - \frac{\partial h}{\partial t}(\psi_+ - \widehat{\psi}) - w^s(\psi_+ - \psi_0) = \overline{w'\psi'}_0 - \overline{w'\psi'}_+ + hS_\psi \tag{3}$$

where the subscript denotes the location at which an expression is evaluated, $+$ denoting the height $z = h^+$, and 0 denoting the atmospheric level just above the surface.

In a typical mixed-layer approach, the homogeneity of ψ in the boundary layer ensures that $\widehat{\psi} = \overline{\psi}_0$. One of the problems in modeling cumulus is that the cloud layer becomes conditionally stable, and therefore ψ is not height-independent in the boundary layer, causing $\widehat{\psi}$ to become another unknown. However, in equilibrium we require $\frac{\partial h}{\partial t} = 0$, such that this problem resolves itself.

2.2 *Bulk conservation equations*

As the sub-cloud layer is typically well-mixed, write $\psi_0 = \psi_m$, the sub-cloud layer value. The entrainment velocity is

$$w^e = \frac{\partial h}{\partial t} + w^s \tag{4}$$

Also, a quasi-steady state implies

$$\frac{\partial}{\partial z}\frac{\partial\overline{\psi}}{\partial t} = 0 \quad \text{and hence} \quad \frac{\partial\widehat{\psi}}{\partial t} = \frac{\partial\psi_m}{\partial t} \tag{5}$$

Utilizing these relationships and using the notation

$$\Delta\psi = \psi_+ - \psi_m \tag{6}$$

equations (3) and (4) can be used to construct an equilibrium bulk model for the thermodynamic boundary layer state as follows ($\psi_m = \{\theta_l, q_t\}$):

$$\frac{\partial h}{\partial t} = 0 = \quad w^e - w^s, \tag{7}$$

$$\frac{\partial\theta_l}{\partial t} = 0 = \quad \frac{w^e\Delta\theta_l + \overline{w'\theta'_l}_0}{h} + S_{\theta_l}, \text{and} \tag{8}$$

$$\frac{\partial q_t}{\partial t} = 0 = \quad \frac{w^e\Delta q_t + \overline{w'q'_t}_0}{h} + S_q, \tag{9}$$

where θ_l and q_t denote the sub-cloud layer values of the liquid water potential temperature and total water content, respectively. Equations (7) to (9) form the basis for often-used boundary layer models (Lilly, 1968; van Driel and Jonker, 2011), mostly in the case of homogeneous, i.e. clear or stratocumulus, boundary layers. In equilibrium at least, these equations are just as valid for the cumulus capped boundary layer. This is because the assumption of quasi-steadiness is enough to arrive at equations (7-9), making the assumption of a 'well-mixed' layer obsolete.

Therefore, these equations are applicable to the average state of the cumulus capped boundary layer as well. In part, though, this merely shifts the complexity into finding an entrainment formulation for w^e which is valid in a cumulus capped boundary layer.

2.3 *Closure: entrainment formulation*

Given the forcings (i.e. fluxes and sources), equations (7) to (9) are closed if a parameterization for w^e can be found. For this, we follow the approach of Stevens (2007) and use the assumption of quasi-steadiness of the boundary layer. In order to exploit this, consider what is sometimes called the 'dry virtual potential temperature' (Lewellen and Lewellen, 2002):

$$\theta_{vd} = \theta_l + \epsilon_I\theta q_t \tag{10}$$

with $\epsilon_I = \frac{R_d}{R_v} - 1$. In the absence of liquid water, θ_{vd} is equal to the virtual potential temperature. As the temperature dependence in the second term is typically negligible, hereafter the dry virtual potential temperature is approximated as a linear relation combination of θ_l and q_t, i.e. $\widetilde{\epsilon_I} \equiv \epsilon_I\theta \approx$ constant.

In this approximation, the use of θ_{vd} has two advantages. First, its turbulent flux

$$\overline{w'\theta'_{vd}}(z) = \overline{w'\theta'_l}(z) + \widetilde{\epsilon_I}\overline{w'q'_t}(z) \tag{11}$$

reduces to the virtual potential temperature flux in the sub-cloud layer. The profile of the sub-cloud layer virtual potential temperature flux is often assumed to behave analogous to that of the clear boundary layer, such that the top flux relates to the surface flux with a certain efficiency κ (Ball, 1960; Betts, 1973), i.e.

$$\overline{w'\theta'_{vd}}(\eta) = -\kappa\overline{w'\theta'_{vd}}(0) \tag{12}$$

where η denotes the sub-cloud layer top, and κ has a value of approximately 0.25.

Secondly, as a linear combination of θ_l and q_t, the exact same conservation equations can be deduced for θ_{vd} as were used for liquid water potential temperature and humidity. To see this, repeat the bulk analysis performed above twice, once integrating from $z = 0$ to $z = h^+$ (repeating the result above) and once from 0 to η, now for $\psi = \theta_{vd}$. The resulting equations are, respectively:

$$\frac{\partial\theta_{vd}}{\partial t} = \frac{w^e\Delta\theta_{vd} + \overline{w'\theta'_{vd}}(0)}{h} + S_{\theta_{vd}} \quad \text{and} \tag{13}$$

$$\frac{\partial\theta_{vd}}{\partial t} = \frac{\overline{w'\theta'_{vd}}(0) - \overline{w'\theta'_{vd}}(\eta)}{\eta} + S_{\theta_{vd}} \tag{14}$$

Since quasi-steadiness requires the two time-derivatives to be equal, the entrainment velocity has to satisfy

$$w^e = \frac{\overline{w'\theta'_{vd0}}}{\Delta\theta_{vd}}\left[(1+\kappa)\frac{h}{\eta} - 1\right] \quad \text{for} \quad h \geq \eta \tag{15}$$

which follows from combining equations (12) to (14).

When the lifting condensation level exceeds the boundary layer height, no clouds will form, and therefore the sub-cloud layer height reduces to the boundary layer

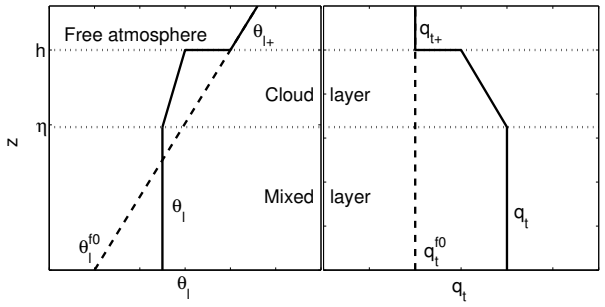

FIG. 1: Schematic picture of the connection between the idealized 'free atmosphere', extending from above the boundary layer all the way up to the ground (dashed lines), and the actual profile of the atmosphere, with a boundary layer up to $z = h$ (solid line). The boundary layer is divided into a well-mixed part and a cloudy part. In this paper, the 'jump' is considered the difference between the value above the boundary layer $(+)$ and the mixed-layer value.

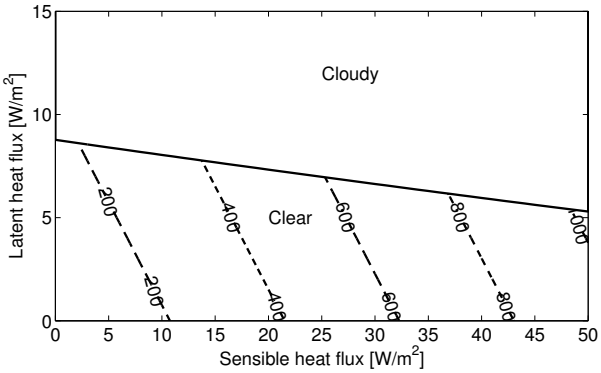

FIG. 2: The threshold of clear and cloudy equilibrium solutions as a function of surface fluxes for $\theta_l^{f0} = 285$ K, $q_t^{f0} = 5$ g/kg, $\Gamma = 6$ K/km and a subsidence of $w^s = 1$ cm/s. The dashed lines indicate clear boundary layer height, the solid line is the threshold after which clouds form.

height. In this situation, $h^+ = \eta^+$ and equations (13) and (14) become identical. For the case of $h = \eta$, equation (15) reduces to:

$$w^e = \kappa \frac{\overline{w'\theta'_{vd0}}}{\Delta\theta_{vd}} \quad \text{for} \quad h = \eta \tag{16}$$

which is exactly the entrainment formulation of the well-known (Lilly, 1968) flux-jump entrainment relation used for the clear boundary layer. Therefore, equations (7) to (9) with (15) to (16) extend the clear boundary layer mixed layer model framework to the cumulus situation. The model solves for the prognostic variables $\{h, q_t, \theta_l\}$, driven by the forcings $\{\overline{w'\theta'_{l0}},\ \overline{w'q'_{t0}},\ S_{\theta_l},\ S_q,\ w^s,\ p_s\}$, which are assumed known. The surface pressure p_s is used to calculate the saturation curve, needed later.

3. EQUILIBRIUM SOLUTION

In order to investigate the model's behavior, we need an environment. To describe this environment in a very simple yet generic way, we define the free atmospheric profiles as the profile the troposphere would have, would there be no boundary layer (extrapolating downward). The formation of the boundary layer can alter these profiles only up to the boundary layer height h, such that a top boundary condition is automatically supplied, even for time-dependent situations. Now consider the following idealized free atmospheric profiles (dashed lines in Fig. 1)

$$\theta_l^f(z) = \theta_l^{f0} + \Gamma z \quad \text{and} \tag{17}$$

$$q_t^f(z) = q_t^{f0} \tag{18}$$

In the current idealized framework, these profiles can be kept time-independent by compensating the subsidence with radiative cooling as $S_{\theta_l} = -w^s\Gamma$, and setting $S_q = 0$. Note that with the definitions (17,18) of the free atmosphere, the jumps $\Delta\psi = \psi_+ - \psi_m = \psi^f(h) - \psi_m$ are defined by the sub-cloud value and the boundary layer height h.

A schematic picture of this notion is drawn in figure 1, illustrating how this idealized free-atmosphere is defined in relation to the sub-cloud atmospheric value. Figure 1 illustrates how this definition provides a top boundary condition, as it defines the ψ_+ as a function of boundary layer height. Note that although the profiles of θ_l and q_t are drawn with a conditionally stable cloud-layer lapse rate, these lapse rates are not prognostically needed for the model dynamics.

This allows equations (7–9) to be solved for the equilibrium case as follows,

$$\theta_l^\infty = \theta_l^{f0} + \frac{\overline{w'\theta'_{l0}}}{w^s} \quad \text{and} \tag{19}$$

$$q_t^\infty = q_t^{f0} + \frac{\overline{w'q'_{t0}}}{w^s} \tag{20}$$

where the superscript ∞ denotes the equilibrium ($t \to \infty$) value. The current framework thus allows a simple analytical solution for the sub-cloud layer values, even though the behavior in the cloud layer is unsolved for. Note that these values are valid in both cloudless and cumulus regimes.

We stress the importance of equation (7), from which it becomes apparent that $w^e = w^s$ in steady state, independent of the closure or case. This causes equations (19–20) to be valid always, regardless of entrainment formulation.

3.1 *Cloudy threshold*

The third variable for which an equilibrium solution can be solved is η, as can be directly deducted from combining equations (12) and (14):

$$\eta^\infty = -\frac{\overline{w'\theta'_{vd0}}\,(1+\kappa)}{S_{\theta_{vd}}} \tag{21}$$

(where in the present case $S_{\theta_{vd}} = -w^s\Gamma$). In cloudless situations, $h = \eta$ and the above equilibrium solution reduces to the equilibrium mixed-layer solution for the clear boundary layer with constant subsidence, as studied by van Driel and Jonker (2011). They showed that this steady state solution is unique and unconditionally stable.

Equations (19) to (21) define whether or not the forcings support a cloud deck for $t \to \infty$, regardless of the current boundary layer state. This follows from the fact that θ_l^∞ and q_t^∞, together with p_s, unambiguously define the equilibrium lifting condensation level $\mathcal{L}^\infty$:

$$\mathcal{L}^\infty = f(\theta_l^\infty, q_t^\infty, p_s) \tag{22}$$

by solving for the height at which $q_{sat}(\theta_l^\infty, p_s) = q_t^\infty$.

It is important to note that, in this work, the sub-cloud layer height η is distinguished from the lifting condensation level $\mathcal{L}$, even in the case of a cumulus layer. This is because, in contrast to typical bulk models, they do not necessarily have to equal, at least not in the equilibrium sense. In fact, the equilibrium lifting condensation level following from θ_l^∞ and q_t^∞ as given by equations (19–20) is generally not equal to η^∞ as given by equation (21), i.e. $\mathcal{L}^\infty \neq \eta^\infty$.

Note that discrepancy, and particularly equation (21) is not a new consideration, but was already noted by Betts and Ridgway (1989), who recognized its importance for future work. In this work, we attempt to give a physical interpretation to how the boundary layer reacts as a function of η^∞ and $\mathcal{L}^\infty$. Comparison of η^∞ and $\mathcal{L}^\infty$ allows us to identify different dynamical regimes, which can even be related to equilibrium cloud types.

To illustrate the behavior of η^∞, figure 2 shows a phase-space of sensible and latent heat surface fluxes, given some arbitrary values defining the free atmosphere and subsidence. Note that as η^∞ is defined by the buoyancy flux, it feels the sensible heat flux stronger than the latent heat flux, and therefore the sub-cloud layer height grows mostly with sensible heat flux. A threshold is crossed for $\mathcal{L}^\infty < \eta^\infty$, after which clouds can exists. Below this threshold, η^∞ represents the actual boundary-layer height in equilibrium.

4. LES CASE DESCRIPTION

In order to be able to better appreciate further results predicted by the model framework, a number of Large Eddy Simulations (LES) are performed with equal forcings and conditions. Large Eddy Simulations can be used to simulate the boundary layer processes in detail, while the forcings and initial profiles can be arbitrarily set. For this research, all simulations have been performed using GALES, the GPU-resident version of the Dutch Atmospheric Large Eddy Simulation (Schalkwijk et al., 2011). Using GPU acceleration allows the simulations to be performed locally, such that new simulations can be quickly run with different forcings. Also, the graphical representation of the present clouds provides rapid feedback on the current boundary layer state.

All simulations are performed on a domain of 6.4 km in both horizontal directions and 3.06km in the vertical direction. Grid spacing is 24m in the vertical and 50m in the horizontal direction. The simulations are performed with constant prescribed surface fluxes for θ_l and q_t, and constant and prescribed radiative cooling and subsidence profiles. No geostrophic wind is present, in accordance with the model framework. Parameterized longwave radiative cooling is applied in all simulations, although it is assumed negligible in the model.

5. CLOUD REGIMES

As explained in section 3, we do not assume η and $\mathcal{L}$ equal in this framework. By treating η^∞ and $\mathcal{L}$ separately, we are able to distinguish different dynamical regimes by considering the buoyancy flux in the sub-cloud layer.

Interesting in this context is that the solution for η^∞ (equation 21), follows from *dynamical* arguments (equation 14). In contrast, the lifting condensation level is inherently a *thermodynamical* property of the boundary layer. Besides being a further argument for the distinction between η and $\mathcal{L}$, this reasoning can be applied in the model framework for further interpretation.

Before continuing, we again refer to Betts and Ridgway (1989), who, after establishing equation (14), also noted that the entrainment efficiency κ in the sub-cloud layer (equation 12) seems to be less of an established concept in the cumulus case than it is in the case of the clear boundary layer.

This work proposes that the conflict between thermodynamical and dynamical behavior in the sub-cloud layer is the cause of variation in κ (and therefore the supposed uncertainty of equation (12)), For this, we present a very simple argument combining the dynamical and thermodynamical tendency.

We propose that the dynamical behavior of the virtual potential temperature flux is governed by equation (12), as quasi-steadiness implies that equation (14) can be rewritten to:

$$\left[\frac{\partial \overline{w'\theta_v'}}{\partial z}\right]_{sub-cloud}^{\infty} = -\frac{\overline{w'\theta_{v0}'}(1+\kappa^\infty)}{\eta^\infty} \tag{23}$$

where κ has been replaced by κ^∞ to denote it is the κ-value corresponding to the limiting case of η^∞. Note that the dynamical behavior of the sub-cloud layer now is determined by the entrainment efficiency, as this determines the *slope* of the buoyancy flux.

Now, when the lifting condensation level $\mathcal{L}^\infty$ falls below η^∞, clouds form from this level onward, thereby increasing the buoyancy flux due to the liquid water component. This causes the minimum buoyancy flux, found just below the lifting condensation level, to be always smaller in magnitude than $\kappa^\infty\ \overline{w'\theta_{v0}'}$. Figure 3 sketches this approach in the left panel, but also shows LES evidence on the right panel, from a case with arbitrary, but constant, surface fluxes and radiative forcings, started from free atmospheric profiles as equations (17) and (18). This is a single LES case from a large number of similar cases

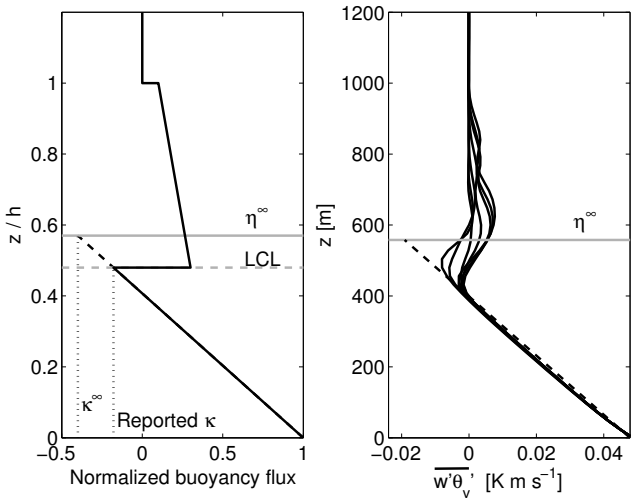

FIG. 3: Figure illustrating the dynamics of the buoyancy flux as it is governed by a combination of the equilibrium sub-cloud layer height η^∞ and the current lifting condensation level $\mathcal{L}$. On the left, a schematic illustration shows how the buoyancy flux slope and minimum in the sub-cloud layer behave, which is complemented by results from a Large-Eddy Simulation on the right panel. The LES profiles are results from a growing cumulus layer case, started in idealized free-atmospheric profiles and performed with constant surface fluxes and sources. Shown are hourly averaged flux profiles at 10h, 20h, 30h, ..., 80h: notice how the slopes overlap in the lower boundary layer.

which will be described in subsection 5.4 which typically show similar behavior. Note how the LES profiles change, including the minimum buoyancy flux, as the lifting condensation level varies with time, but how the slope in the lower part of the boundary layer remains very steady.

We have found κ^∞ to be approximately equal to 0.4, empirically based on the large number of LES cases performed. Note that while this value might seem large, we emphasize that this value sets the *slope* of the buoyancy flux, such that the minimum buoyancy flux is always *larger* than $-\kappa^\infty \ \overline{w'\theta'_{v0}}$. In fact, if one were to define an *effective* entrainment efficiency $\kappa^{eff} = -\overline{w'\theta'_v}^{min} / \overline{w'\theta'_{v0}}$, one would typically find κ^{eff} around 0.2. This is illustrated by figure 3.

As the equilibrium behavior of the buoyancy flux is thus controlled by an interplay between the lifting condensation level $\mathcal{L}^\infty$ and the sub-cloud layer height η^∞ in equilibrium, we can now identify three different dynamical regimes which show distinctly different behavior in the virtual potential temperature flux, which can be directly related to boundary layer behavior.

5.1 *Regime I:* $\mathcal{L}^\infty > \eta^\infty$ *– Clear layer*

In this case, the lifting condensation level lies above the mixed layer height. This is the simplest regime, depicted as the region below the solid line in figure 2. The behavior of which has been described above: no clouds can form, and a clear boundary layer will develop with a boundary layer height of $h^\infty = \eta^\infty$. The model reduces to the mixed layer model as studied by van Driel and Jonker (2011).

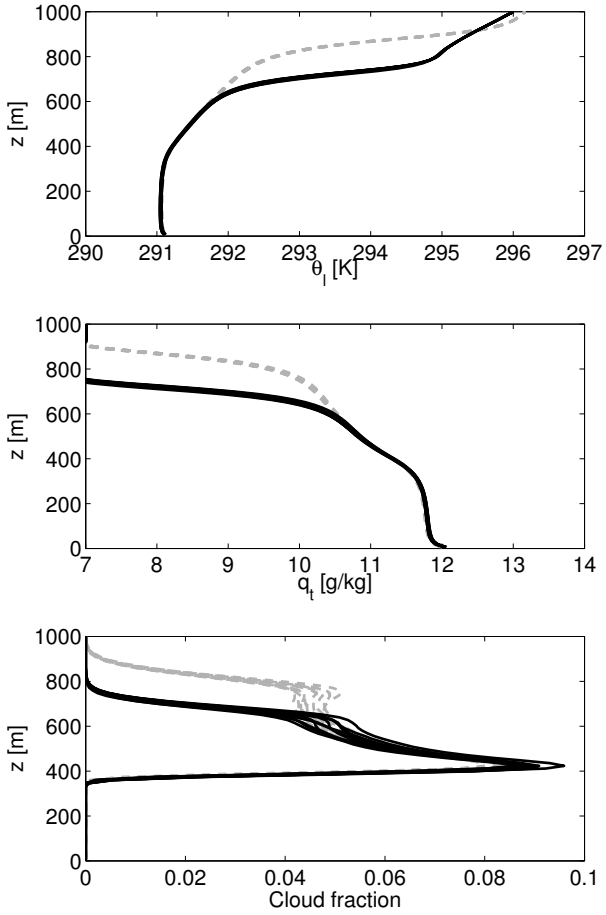

FIG. 4: Demonstration of two steady state cumulus cases, achieved given arbitrary environmental parameters and forcings. Plotted are 10 hours (5^{th} - 15^{th} hours of simulated time) of hourly averaged liquid water potential temperature, water content and cloud fraction profiles, in which nearly no time-dependence is seen. The dashed gray profiles depict a simulation started with 100m higher initial inversion.

5.2 *Regime II:* $\eta^\infty > (1+\kappa^\infty)\mathcal{L}^\infty$ *– Coupled layers*

Outside of regime I, the lifting condensation level appears below the mixed layer height and clouds are thus allowed to form. Careful inspection of figure 3 reveals another regime division, however. Note that in particular moist environments, the fraction $\mathcal{L}^\infty / \eta^\infty$ might be such that the minimum buoyancy flux will not drop below zero:

$$\overline{w'\theta'_v}^{min} \geq 0 \quad \text{for} \quad \frac{\eta^\infty}{\mathcal{L}^\infty} \geq (1+\kappa^\infty) \tag{24}$$

Observations suggest (de Roode and Duynkerke, 1997) that the degree of coupling is important in regulating the

amount of moisture transport into the cloud layer. Among other reasons, this causes the cloud-base (minimum) buoyancy flux to be considered (Bretherton and Wyant, 1997; Stevens, 2000) an important parameter when considering the boundary between cumulus and stratocumulus. A negative cloud base buoyancy flux then typically implies decoupling of the sub-cloud and the cloud-layer, which is characteristic for a cumulus deck. Therefore, the value of the negative buoyancy flux allows the separation of cloud types which will form in the boundary layer.

For this reason, we expect that for the current regime, where the environment is moist enough to prevent the minimum buoyancy flux to drop below zero, the equilibrium state will couple with the cloud layer, such that no equilibrium cumulus layer can form. In fact, it is likely the layer will tend to stratocumulus in this regime. At that point, however, the liquid water content will become so high that long-wave radiative cooling of the cloud layer is no longer negligible, such that the entrainment formulation of (15) is no longer applicable. A future possibility might be to couple the entrainment formulation to currently used stratocumulus entrainment formulations (Moeng, 2000; Nicholls and Turton, 1986), but for now, further investigation of the coupled layer state remains outside the scope of this paper.

5.3 *Regime III:* $\mathcal{L}^\infty < \eta^\infty < (1+\kappa)\mathcal{L}^\infty$ *– Decoupled layers*

The last regime then, is the regime where a negative minimum buoyancy flux occurs:

$$\overline{w'\theta_v'}^{min} \leq 0 \quad \text{for} \quad \frac{\eta^\infty}{\mathcal{L}^\infty} \leq (1+\kappa) \tag{25}$$

while still $\eta^\infty > \mathcal{L}^\infty$ (a negative minimum buoyancy flux also occurs in the clear boundary layer). This will result in decoupling between the sub-cloud layer and the cloud-layer, causing a steady cumulus deck to form for $t \to \infty$. This regime therefore spans the range for which steady state cumulus can occur.

The current model framework works much like the clear boundary layer mixed layer model, but is extended by regarding the cumulus layer as a large 'entrainment zone' (Stevens, 2007). As a result, the model gives little information on the cloud layer itself. For example, the model does not provide information on the lapse rates of temperature and humidity in the cloud layer, nor does it provide information on cloud cover or liquid water content. Probably, at least some of these variables can be added to the model, but at the cost of increased complexity. In this work, the model is kept as simple as possible to focus on the behavior of the boundary layer state.

A rather surprising result of the model is that no *unique* value is predicted for the equilibrium cloud depth h^∞ in terms of the model parameters. Indeed, the quasi-equilibrium behavior described in equations (13) and (14) defines a steady state independent of cloud layer depth; this implies that the equilibrium cloud layer depth is not unique and will depend on the initial conditions. A more mathematical explanation for this fact is found in the appendix. Do note that this is a result of the assumption of quasi-equilibrium behavior, and not of the constant subsidence profile, as it can be shown to occur for an arbitrary subsidence profile.

One of the illustrative possibilities now then, is that the model provides the opportunity to set-up an idealized steady state cumulus case for arbitrary forcings. An example of such an idealized LES case is shown in figure 4, where an LES is initialized as a simple mixed layer with some initial height $h > \eta^\infty$, with θ_l and q_t in the mixed layer chosen such that equations (19) and (20) are satisfied. As this state is very close to the predicted cumulus steady state, the simulation reaches a steady state in only five hours of simulated time. Figure 4 shows hourly averaged profiles for the 5^{th} to 15^{th} hour of simulated time. Note that these profiles nearly perfectly overlap, demonstrating the steadiness of the case.

To show the non-uniqueness of the equilibrium cloud depth, a second case was set up in exactly the same manner, yet with a slightly higher initial inversion. The results of this case are shown in figure 4 in dashed gray lines. Note that this case also ends up in exactly the same equilibrium state in mixed layer temperature and humidity (even lower cloud fraction) but finds its equilibrium with a thicker cloud deck than the first case, illustrating our point.

By using such *generalized* steady state cumulus cases, further studies could more easily investigate the influences of the parameters important to describing the cumulus layer than by using a pre-defined case like BOMEX (Siebesma et al., 2003, more about this later). For example, the differences in behavior of steady state cumulus at sub-cloud temperatures between 290 K and 292 K can be quickly compared.

5.4 *Phase-space*

In order to illustratively combine the regimes described above in a phase-space of surface fluxes, we describe the surface fluxes by the surface heat flux $\rho c_p \overline{w'\theta_{v0}'}$ (W m^{-2}) and the Bowen ratio β

$$\beta = \frac{c_p}{L_v}\frac{\overline{w'\theta_{l0}'}}{\overline{w'q_{t0}'}} \tag{26}$$

with c_p the specific heat capacity of water and L_v the latent heat of vaporization. The Bowen ratio describes how the surface heat flux is divided over latent and sensible heat. Combined, the total surface heat flux $\rho c_p \overline{w'\theta_{v0}'}$ describes how much energy is brought into the boundary layer from the surface, and thereby sets η^∞. The Bowen ratio describes how this energy is divided over moisture and temperature, and thus governs the lifting condensation level.

The cloud regimes are shown in the surface flux phasespace in figure 5, which illustrates where the cumulus, stratocumulus and clear boundary layer states are expected by the model in solid lines. To verify the model predictions, a number of Large Eddy Simulations are performed, each starting at the idealized free atmospheric

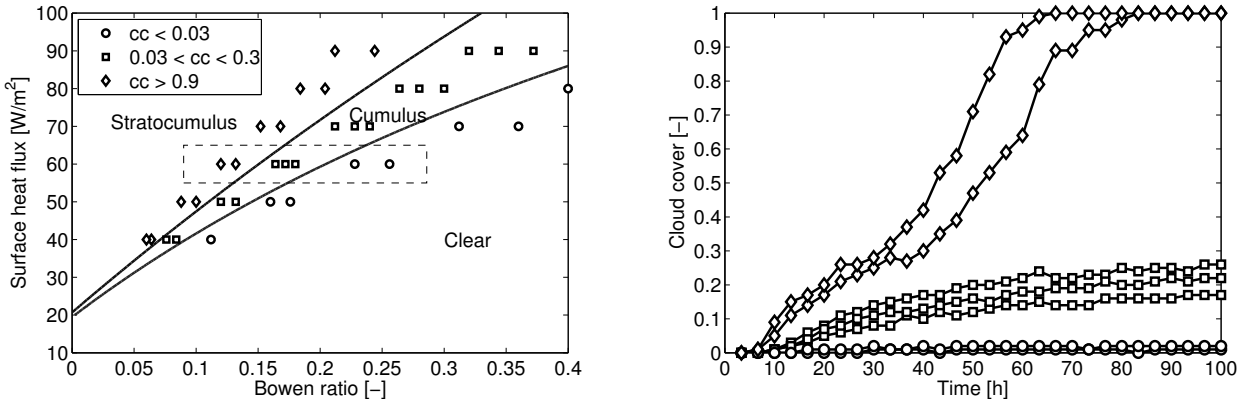

FIG. 5: Left panel: the cloud type regimes in a phasespace of surface flux strength and composition for $\theta_l^{f0} = 290$ K, $q_t^{f0} = 8$ g/kg, $\Gamma = 6$ K/km and $w^s = 2$ cm/s. Solid lines separate the cloud regimes according to the model framework, while the overlaid symbols each depict the state of an LES simulation after 100 hours of simulated time. Right panel: Time series of the simulations contained in the dashed rectangle in the left panel, showing how the cloud cover evolves from the idealized free atmospheric state at $t = 0$ to the equilibrium state at $t = 100h$.

state according to equations (17) and (17) with $\theta_l^{f0} = 290$ K, $q_t^{f0} = 8$ g/kg, $\Gamma = 6$ K/km and $w^s = 2$ cm/s, thus without initial boundary layer. We would like to emphasize that *each simulation started from the exact same initial conditions*; only the values of the surface fluxes differ. The simulations are performed for 100 hours with constant forcings to allow the simulations to reach equilibrium. The symbols in figure 5 each represent a separate LES simulation, and the type of symbol depicts the average cloud cover in the last hour of the simulation, which allows the distinction between cumulus, stratocumulus and clear boundary layers.

It is remarkable how each LES simulation ends in the predicted state, while each started from the same initial conditions. The right panel of figure 5 shows the time series of cloud cover for some selected simulations with equal surface heat flux. This panel clearly shows how the cases with large Bowen ratios cannot develop a cloud cover, the cases with intermediate Bowen ratios develop a cumulus layer and the cases with low Bowen ratio develop a cumulus layer which then evolves into a stratocumulus layer.

Note that as expected, the model breaks down in the region of fully coupled layers, as the increase in cloud fraction increases the effect of radiative cooling to a point at which this is no longer negligible. Therefore, the region of 'stratocumulus' should not be taken too literally, but rather as the breakdown point of the model. Often, simulations do not converge to a steady state at this point, but rather keep growing, much alike the behavior witnessed by Bellon and Stevens (2011). This might be an artefact of the constant subsidence profile, however, which cannot compensate for increased entrainment as radiative cooling increases. Nevertheless, all LES simulations performed in this region develop a layer in which the cloud cover is 100%.

The model thus seems to allow for the prediction of the equilibrium cumulus regime *a priori*, irrespective of initial conditions, which is confirmed by LES results.

6. SEA SURFACE TEMPERATURE

One could argue that the above approach of assuming constant surface fluxes is rather unrealistic, even in the equilibrium limit. For one, such an approach neglects the dynamical feedback which does occur when fluxes are the result of the difference between the boundary layer state and the surface properties. An interesting approach, therefore, is to allow this feedbacks in the fluxes to occur by allowing some surface-atmosphere interaction. A simplified example of such a system can be found by writing the surface fluxes as

$$\overline{w'\theta'_{l0}} = V(\theta_{SST} - \theta_l) \tag{27}$$

$$\overline{w'q'_{t0}} = V(q^S_{sat} - q_t) \tag{28}$$

where θ_{SST} the sea surface potential temperature and q^S_{sat} the saturation humidity at sea surface temperature. In this approach, V represents some transfer coefficient, which is assumed constant at 1 cm/s.

Note that when this surface parameterization is implemented into the equations (7) to (9), the steady state solutions (19) and (20) are still valid and can be expanded into

$$\theta_l^\infty = \frac{w^s \theta_l^{f0} + V\theta_{SST}}{w^s + V} \tag{29}$$

$$q_t^\infty = \frac{w^s q_t^{f0} + V q^S_{sat}}{w^s + V} \tag{30}$$

revealing an interesting combination of surface and top restraints on the boundary layer. Still assuming θ_{vd} a linear combination of θ_l and q_t, these equilibrium solutions can be combined with equations (10) to find the equilib-

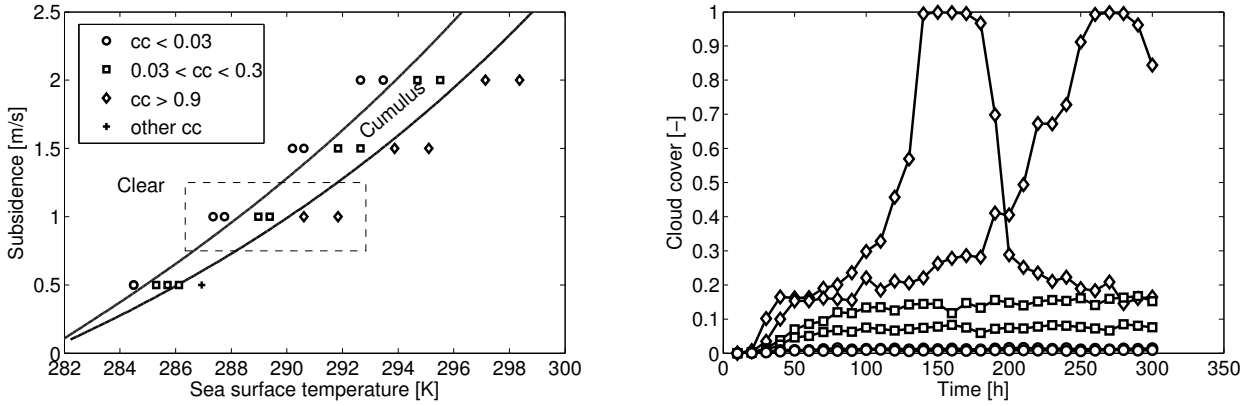

FIG. 6: The phase-space cloud regime scan of figure 5 is repeated for the case of constant sea surface temperature, as a function of temperature and subsidence. Other parameters are set to $\theta_l^{f0} = 280$ K, $q_t^{f0} = 0$ g/kg, $\Gamma = 6$ K/km and V = 1 cm/s. Solid lines separate the cloud regimes based on equilibrium lifting condensation level and subcloud layer height. Symbols denote the maximum hourly-averaged LES cloud cover.

rium buoyancy flux as follows

$$\overline{w'\theta'_{vd0}}^{\infty} = \frac{w^s V}{w^s + V}\left(\theta_{vd,SST} - \theta_{vd}^{f0}\right) \tag{31}$$

where $\theta_{vd,SST} = \theta_{SST} + \tilde{\epsilon_I} q_{sat}^S$ represents the sea surface 'virtual potential temperature'. Combining equation (31) with equation (21), we can express η^{∞} as a function of the sea surface temperature as follows.

$$\eta^{\infty} = -\frac{w^s V}{w^s + V}\frac{\left(\theta_{vd,SST} - \theta_{vd}^{f0}\right)(1 + \kappa^{\infty})}{S_{\theta_{vd}}} \tag{32}$$

This completes the steady state solution in the case of interaction with a constant sea surface, such that the phase-space of figure 5 can be transformed to a phase-space of θ_{SST} and θ_{f0}. Indeed, the phase-space scan of the previous section can be repeated, now including the sea surface feedback mechanism.

In order to perform this scan, we simplified the LES sea surface feedback to behave exactly like prescribed by equations (27-28). This allows us to focus on the effects of adding this mechanism, without adding complicated feedbacks like wind velocity feedbacks.

The result is displayed in figure 6. We have chosen to scan a phase-space of sea surface temperature and subsidence, as this allowed us to perform all LES simulations, like before, starting from the exact same initial conditions. Only sea surface temperature, subsidence and radiative forcing (such that always $S_{\theta_l} = -w^s\Gamma$) were varied between simulations. The simulations were now run for $300h$ to allow the extra feedbacks to settle.

Note that the cloud types are mirrored with respect to figure 5, as coupling now occurs on the bottom right hand side, with high sea surface temperature and relatively little subsidence. This can be understood by realizing the saturation equation is non-linear in such a way that relatively, the latent heat flux reacts more strongly to an increased SST than the sensible heat flux does.

Once again, the model is able to provide a surprisingly good outline of the area in the phase-space where cumulus occurs. This is especially true considering the model does not take the actual dynamics of the feedbacks in account. It seems that by considering the equilibrium solution we can achieve a good feeling of the state the system strives to dynamically as well.

In the coupling regime, another interesting phenomenon occurs, which is most visible in the right panel of figure 6. It seems that whereas the coupled regime was unsteady in figure 5 in the sense that the boundary layer height never stopped increasing, the coupled state in this system is unsteady in another sense. In many cases which tend to couple and form an unbroken cloud deck, the system suddenly becomes unstable and falls back to a state of a broken cloud deck or even a cloudless state. The event seems to be due to the newly introduced sea surface feedback, as it does not seem to occur in the cases of constant surface fluxes. This might be an artefact of the simplified case set-up or a real phenomenon. More simulations, likely incorporating a more realistic radiation scheme, are needed to better appreciate this phenomenon. For now it suffices to note that the decoupled-coupled regime division seems to mark the end of the region where 'normal' cumulus layer evolution occurs. In order to distinguish the steady cumulus cases with these unsteady cases, the symbols in figure 6 denote the maximum hourly-averaged cloud cover instead of the cloud-cover of the last simulated hour.

7. INTERCOMPARISON CUMULUS CASES

In order to evaluate the model performance in the context of other studies, we look specifically to studies focused on the atmospheric boundary layer, with models and observations to backup the findings. For this reason, this section relates the model output to LES model intercomparison cases, as these studies provide a wealth of data

and are easily reproduced by our LES model.

Considering that most LES simulations use periodic boundary conditions, no true large-scale advection is possible. Instead, the effects of large-scale advection are included in source terms. For this reason, in the appendix we generalize the model to include for non-constant, but still horizontally homogeneous, sources, as well as a more general divergence. This allows the model to be compared with well-known intercomparison cases, to evaluate its use in slightly less idealized situations. Do note that wind shear does, in fact, have effects on the entrainment relations, not included in the model. These effects are assumed negligible in this section.

Two well-known intercomparison cumulus cases are the Barbados Oceanographic Meteorological EXperiment (BOMEX, Siebesma et al., 2003) and the Rain In Cumulus over the Ocean (RICO, Abel and Shipway, 2007) cases. Figure 7 shows the phasespaces created using the generalized model in the appendix, and the spot the cases are situated in. The region in phasespace where equilibrium cumulus is expected is shaded in light gray.

The BOMEX case is typically run with constant surface fluxes, and is therefore shown in a phasespace of surface fluxes. Note that BOMEX was originally designed as a steady state cumulus case, which is confirmed by the present model as it situates BOMEX in the cumulus regime (Fig. 7). This is further confirmation of the model performance, also in more general cases.

The RICO forcings are a little less obvious to model, as the RICO case is typically run with a forced sea surface temperature, dependent on wind velocity through surface drag. Running the original case in LES using $V = C_D U_{10m}$, the transport coefficient is determined by a drag coefficient and the wind velocity at 10m, we have to relate this to the model using a constant V. We chose a constant V to best represent the surface fluxes the LES produced. For the RICO case, we found a numerical value of $V = 0.8$ cm/s. Using this value, the right panel of figure 7 shows the RICO case in a phasespace of sea surface temperature and free atmospheric temperature. Interesting to note is that the RICO case seems to be found in the model's coupled regime. The fact that RICO remains in a cumulus state might actually be caused by precipitation, which acts as a sink for moisture in the boundary layer. Indeed, simulations have been found to depend sensitively to microphysics (Abel and Shipway, 2007). This illustrates the end of the model's applicability, of course, although it might be possible to implement a simple precipitation model.

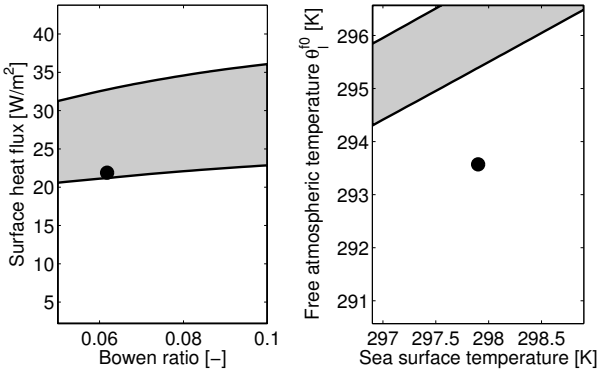

FIG. 7: Intercomparison cases BOMEX (left panel) and RICO (right panel) shown in their respective phasespace surroundings.

8. CONCLUSIONS AND OUTLOOK

The developed modeling framework is thus a relatively easy extension to the well-known mixed layer model for the convective boundary layer, closed using linearity of fluxes throughout the boundary layer. Equilibrium states can be predicted in a phase-space of environmental forcings (i.e. free atmospheric conditions, radiative and surface forcings), requiring little knowledge of initial conditions.

The equilibrium cumulus cloud regime can be distinguished on the basis of the minimum buoyancy flux, which can be predicted *a priori* using the model's equilibrium solutions. These cloud regimes are well in accordance with LES evidence, and are set by an interplay of surface and free atmospheric forcings. The equilibrium cumulus regime is found in between the clear and coupled regimes, sensitively dependent on the ratio between sensible and latent heat fluxes at the surface, but also on the state of free atmospheric air above the boundary layer.

LES cases set-up with the model's equilibrium solutions as initial conditions remain in steady state, thereby providing an easy methodology for equilibrium studies. As an outlook, the model might be used to quickly set up LES equilibrium studies in any given point in the phasespace of possible forcings, allowing a detailed study of cloud characteristics as a function of forcing parameters. Possible examples include studies of cloud organization as a function of surface forcings, or further quantification in lateral cloud entrainment and detrainment in steady state. The modeling framework presented here can also be further extended by including, for example, cloud cover or mass flux in the model dynamics, which might aid in deepening our understanding of the cloud capped boundary layer.

Besides equilibrium studies, mixed layer modeling has also shown good performance in time-dependent cases (e.g. van Driel and Jonker, 2011). For this reason, future applications in time-dependent cloud phenomena and regime transitions are in scope, as well, although these would require further assumptions regarding the cloud layer conditional lapse rate.

A. LINEAR STABILITY ANALYSIS

The stability of equations (7) to (9) can be most easily evaluated if the coordinate system is chosen such that it is easily diagonalized. This is most easily done when we

choose $\{h, \theta_{vd}, \chi\}$ as the prognostic variables, in which χ is given as:

$$\chi = \theta_l - \epsilon_I \theta q_t \tag{33}$$

such that it is independent of θ_{vd}, i.e. $\frac{\partial \chi}{\partial \theta_{vd}} = 0$. The system of equations then becomes:

$$\frac{\partial h}{\partial t} = w^e - w^s \tag{34}$$

$$\frac{\partial \theta_{vd}}{\partial t} = \frac{\overline{w'\theta'_{vd0}}(1+\kappa)}{\eta} - w^s \Gamma \tag{35}$$

$$\frac{\partial \chi}{\partial t} = \frac{\overline{w'\chi'}_0 + w^e \Delta\chi}{h} - w^s \Gamma \tag{36}$$

$$\tag{37}$$

Note that the sources are chosen as before, explained after equations (19) and (20). In vector form, this system becomes:

$$\frac{\partial \overrightarrow{x}}{\partial t} = \mathbf{F}\left(\overrightarrow{x}\right) \tag{38}$$

Which can be linearized around some equilibrium value $\overrightarrow{x} = \overrightarrow{x^\infty}$ (for details see van Driel and Jonker (2011)) as follows:

$$\frac{\partial \overrightarrow{x'}}{\partial t} = \mathbf{J}\left(\overrightarrow{x^\infty}\right) \overrightarrow{x'} \tag{39}$$

where $\overrightarrow{x'} = \overrightarrow{x} - \overrightarrow{x^\infty}$, since $\overrightarrow{F}\left(\overrightarrow{x^\infty}\right) = \overrightarrow{0}$. Hence, in the vicinity of the equilibrium state, the behavior of the system is governed by the Jacobian $\mathbf{J}$ evaluated in equilibrium.

The general Jacobian of this system is quite complex and outside the scope of this appendix, but it can be reduced by taking evaluating it in equilibrium and considering a special case.

For one, the system of equations should reduce to a mixed layer model for the clear boundary layer in the case that $\eta = h$ and the entrainment is given by equation (16). Indeed, in this case the equilibrium Jacobian reduces to:

$$\mathbf{J}^\infty = \begin{pmatrix} \frac{\partial w^e}{\partial h} & \frac{\partial w^e}{\partial \theta_{vd}} & 0 \\ -\frac{\overline{w'\theta'_{vd0}}(1+\kappa)}{(\eta^\infty)^2} & 0 & 0 \\ \frac{\Delta\chi}{h}\frac{\partial w^e}{\partial h} & \frac{\Delta\chi}{h}\frac{\partial w^e}{\partial \theta_{vd}} & -\frac{w^e}{h} \end{pmatrix} \tag{40}$$

which has eigenvalues according to:

$$\lambda_{1,2} = -\frac{\Gamma (w^s)^2}{\overline{w'\theta'_{vd0}}} \frac{1}{2\kappa}\left(1 \pm \sqrt{\frac{1-3\kappa}{1+\kappa}}\right) \tag{41}$$

$$\lambda_3 = -\frac{w^s}{h} \tag{42}$$

Indeed, eigenvalues $\lambda_{1,2}$ are identical to those found by van Driel and Jonker (2011). Interesting is that adding moisture to the system of equations adds a third eigenvalue of w^s/h, corresponding to a relatively large time scale of h/w^s. Hence, the coupled system of moisture and liquid water potential temperature seems to have larger time scales than a system without moisture.

Having shown compatibility with the clear boundary layer, now consider the cumulus regime where $h > \eta$. In this case, with some algebra, the equilibrium Jacobian can be written:

$$\mathbf{J}^\infty = \begin{pmatrix} 0 & \frac{\partial w^e}{\partial \theta_{vd}} & \frac{\partial w^e}{\partial \chi} \\ 0 & -\frac{\overline{w'\theta'_{vd}}(1+\kappa)}{(\eta^\infty)^2}\frac{\partial \eta^\infty}{\partial \theta_{vd}} & 0 \\ 0 & \frac{\Delta\chi}{h}\frac{\partial w^e}{\partial \theta_{vd}} & -\frac{w^e}{h} + \frac{\Delta\chi}{h}\frac{\partial w^e}{\partial \chi} \end{pmatrix} \tag{43}$$

From which it is apparent immediately one eigenvalue is zero, $\lambda_1 = 0$ with corresponding eigenvector

$$\overrightarrow{v}_1 = \begin{pmatrix} 1 \\ 0 \\ 0 \end{pmatrix} \tag{44}$$

which corresponds to boundary layer height. Hence, linear stability analysis indicates the system is neutrally stable in h (stable for every $h^\infty > \eta^\infty$). While in this case, higher order terms might invalidate this conclusion, LES evidence seems to support it (e.g. figure 4). At the least, the timescales involved in variation in h are much larger even than those of temperature and humidity, which already act on timescales on the order of days.

B. GENERALIZING THE MODEL TO INCLUDE SOURCES AND DIVERGENCE

In the case of more general sources and divergence, but still in the absence of advection, it can be shown (Stevens, 2006) that equation (3) can be generalized to:

$$h\frac{\partial \widehat{\psi}}{\partial t} - \left(\frac{\partial h}{\partial t} - \overline{w}_+\right)\Delta\psi = \overline{w'\psi'}_0 - \overline{w'\psi'}_+ + h\widehat{S_\psi(z)} \tag{45}$$

where now the source term $S_\psi(z)$ is now an arbitrary function of height, and the vertical velocity $\overline{w}_+$ at $z = h^+$ has replaced the constant subsidence term. For example, in a situation of constant divergence $\mathcal{D}$, we have $\overline{w}_+ = \mathcal{D}h$. Note that the same assumptions are used as in section 2.

Equation (45) is very similar to equation (3), such that the model equations (7) to (9) can still be used when replacing S_ψ by $\widehat{S_\psi(z)}$ and w^s by $-\overline{w}_+$. Although the entrainment equation (15) does not remain valid since the sources in the cloud layer may differ from that of the mixed layer, the equilibrium equations can easily be reproduced to become

$$\theta_l^\infty = \theta_l^{f0} - \frac{\overline{w'\theta'_l}_0 - \overline{w}_+\Gamma_{\theta_l}h + \int_0^h S_{\theta_l}dz}{\overline{w}_+} \tag{46}$$

$$q_t^\infty = q_t^{f0} - \frac{\overline{w'q'_t}_0 - \overline{w}_+\Gamma_{q_t}h + \int_0^h S_{q_t}dz}{\overline{w}_+} \tag{47}$$

$$\int_0^{\eta^\infty} S_{\theta_{vd}}dz = -\overline{w'\theta'_{vd0}}\,(1+\kappa) \tag{48}$$

Note that equation (48) is an implicit equation for η^∞. As equations (46) and (47) determine $\mathcal{L}^\infty$, the above set of equations allows the determination of cloud types as in figure 5 for general sources and vertical wind profiles. Following the same strategy as in section 6, equations

(46) to (48) can also be rewritten in the case of constant sea surface temperature.

Do note however, that these equations are now dependent on h, while it can be shown that even in this more general framework, there is no unique h^{∞}, i.e. the equilibrium boundary layer height is an initial-value problem. Considering the intercomparison cases, this will be solved by using the current LES given height h. The interpretation, however, is that the supported cloud type is dependent on cloud thickness, i.e. a case with given forcings might accommodate an equilibrium stratocumulus deck if the cloud thickness remains within certain limits, but can only accommodate cumulus afterwards. This seems to be in accordance with observations from, for example, the ASTEX case (Frisch, 1995).

References

Abel S and Shipway B, 2007: A comparison of cloud-resolving model simulations of trade wind cumulus with aircraft observations taken during rico. *Quarterly Journal of the Royal Meteorological Society*, **133 (624)**, 781–794.

Ball F, 1960: Control of inversion height by surface heating. *Quarterly Journal of the Royal Meteorological Society*, **86 (370)**, 483–494.

Bellon G and Stevens B, 2011: Using the sensitivity of large-eddy simulations to evaluate atmospheric-boundary-layer models. *Journal of the Atmospheric Sciences*.

Betts A, 1973: Non-precipitating cumulus convection and its parameterization. *Quarterly Journal of the Royal Meteorological Society*, **99 (419)**, 178–196.

Betts A and Ridgway W, 1989: Climatic equilibrium of the atmospheric convective boundary layer over a tropical ocean. *J. Atmos. Sci*, **46 (7)**, 2621–2641.

Bony S, et al., 2006: How well do we understand and evaluate climate change feedback processes? *Journal of Climate*, **19**, 3445.

Bretherton C and Park S, 2008: A new bulk shallow-cumulus model and implications for penetrative entrainment feedback on updraft buoyancy. *Journal of the Atmospheric Sciences*, **65 (7)**, 2174–2193.

Bretherton C and Wyant M, 1997: Moisture transport, lower-tropospheric stability, and decoupling of cloud-topped boundary layers. *Journal of the atmospheric sciences*, **54 (1)**, 148–167.

de Roode S and Duynkerke P, 1997: Observed lagrangian transition of stratocumulus into cumulus during astex: Mean state and turbulence structure. *Journal of the atmospheric sciences*, **54 (17)**, 2157–2173.

Deardorff JW, 1970: Preliminary results from numerical integrations of the unstable planetary boundary layer. *Journal of Atmospheric Sciences*, **27**, 1209–1210.

Dufresne J and Bony S, 2008: An assessment of the primary sources of spread of global warming estimates from coupled atmosphere-ocean models. *Journal of Climate*, **21 (19)**, 5135–5144.

Frisch A, 1995: The atlantic stratocumulus transition experimentastex. *Bull. Am. Meteorol. Soc*, **76**, 889–903.

Heus T and Jonker H, 2008: Subsiding shells around shallow cumulus clouds. *Journal of the Atmospheric Sciences*, **65 (3)**, 1003–1018.

Lewellen D and Lewellen W, 2002: Entrainment and decoupling relations for cloudy boundary layers. *Journal of the Atmospheric Sciences*, **59 (20)**, 2966–2986.

Lilly D, 1968: Models of cloud-topped mixed layers under a strong inversion. *Quarterly Journal of the Royal Meteorological Society*, **94 (401)**, 292–309.

Moeng C, 2000: Entrainment rate, cloud fraction, and liquid water path of pbl stratocumulus clouds. *Journal of the atmospheric sciences*, **57 (21)**, 3627–3643.

Neggers R, Stevens B, and Neelin J, 2006: A simple equilibrium model for shallow-cumulus-topped mixed layers. *Theoretical and Computational Fluid Dynamics*, **20 (5)**, 305–322.

Nicholls S and Turton J, 1986: An observational study of the structure of stratiform cloud sheets: Part ii. entrainment. *Quarterly Journal of the Royal Meteorological Society*, **112 (472)**, 461–480.

Nuijens L and Stevens B, 2011: The influence of wind speed on shallow marine cumulus convection. *Journal of the Atmospheric Sciences*.

Paluch I, 1979: The entrainment mechanism in colorado cumuli. *Journal of the atmospheric sciences*, **36 (12)**, 2467–2478.

Reuter G and Yau M, 1987: Mixing mechanisms in cumulus congestus clouds. part i: Observations. *Journal of Atmospheric Sciences*, **44**, 781–797.

Schalkwijk J, Griffith E, Post H, and Jonker H, 2011: High performance simulations of turbulent clouds on a desktop pc: exploiting the gpu. *BAMS*.

Siebesma A and Holtslag A, 1996: Model impacts of entrainment and detrainment rates in shallow cumulus convection. *Journal of the atmospheric sciences*, **53 (16)**, 2354–2364.

Siebesma A, et al., 2003: A large eddy simulation intercomparison study of shallow cumulus convection. *Journal of the Atmospheric Sciences*, **60 (10)**, 1201–1219.

Stevens B, 2000: Cloud transitions and decoupling in shear-free stratocumulus-topped boundary layers. *Geophysical research letters*, **27 (16)**, 2557–2560.

Stevens B, 2006: Bulk boundary–layer concepts for simplified models of tropical dynamics. *Theor. Comp. Fluid. Dyn.*, **20**, 279–304.

Stevens B, 2007: On the growth of layers of nonprecipitating cumulus convection. *Journal of the atmospheric sciences*, **64 (8)**, 2916–2931.

Tennekes H, 1973: A model for the dynamics of the inversion above a convective boundary layer. *J. Atmos. Sci.*, **30**, 558–567.

van Driel R and Jonker H, 2011: Convective boundary layers driven by nonstationary surface heat fluxes. *Journal of Atmospheric Sciences*, **68**, 727–738.

Vilà-Guerau de Arellano J, Gioli B, Miglietta F, Jonker HJJ, Baltink HK, Hutjes RWA, and Holtslag AAM, 2004: Entrainment process of carbon dioxide in the atmospheric boundary layer. *Journal of Geophysical Research*, **109**.